

# Multi-Objective Optimization of A Multi-Tooth Flux-Switching Permanent Magnet Machine with HTS Bulks

Huajun Ran, Yunpan Liu\*, Linfeng Wu, and Junye Zhao

*College of Electrical Engineering & New Energy, China Three Gorges University, Yichang, China*

**ABSTRACT:** Flux-switching permanent magnet (FSPM) machine has wide application prospects in aerospace and automotive fields. To enhance the machine's electromagnetic performance, a novel multi-tooth flux-switching permanent magnet (MT-FSPM) machine with high-temperature superconducting (HTS) bulks is proposed. The HTS bulks are arranged in the middle of the stator teeth aimed at diminishing flux leakage and amplifying torque output. The method of stator tooth chamfering and rotor flange is adopted to effectively suppress the torque ripple. Then based on the comprehensive sensitivity analysis, the key design parameters of the machine are layered, and the high sensitivity parameters are optimized by response surface method (RSM) and multi-objective genetic algorithm (MOGA) to obtain the optimal value. Finally, a 6/19 MT-FSPM machine model is established in 2D finite element method (FEM). Comparative analysis with the conventional model indicates a 16.4% increase in output torque and an impressive 796% reduction in torque ripple for the proposed model.

## 1. INTRODUCTION

The performance and commercialization level of high-temperature superconducting (HTS) machine have made significant progress since 2000. HTS machine has obvious advantages in volume, quality, and efficiency, which is an ideal solution for large capacity and high torque density propulsion machine and an ideal choice for high-power direct-drive wind turbine [1–3]. With the development of industry, the demand for high torque and low speed direct drive is increasing. As a stator permanent magnet brushless machine, FSPM machine is usually the preferred machine for such applications due to its high torque, high efficiency, and good heat dissipation capacity [4].

The PM of the conventional FSPM machine is arranged in the stator tooth, and the rotor tooth is a simple salient pole structure, which realizes the flux switching in the three-phase concentrated winding through the rotation of the rotor. Although this configuration can achieve high torque density operation, it results in significant consumption of PM. In order to address the issue of PM usage two FSPM machines with E-type and C-type stator teeth are proposed. Under half of the number of PMs, these two machines can also exhibit higher output torque than conventional FSPM machine at low excitation current [5, 6]. However, as the excitation current increases, the magnetic circuits of these three machines will gradually become saturated, resulting in a decrease in output torque, even lower than that of conventional FSPM machine. The MT-FSPM machine is proposed in [7] with half of the PM of the conventional FSPM machine, and it can exhibit higher torque density at low excitation current. Therefore, many experts and scholars have developed a variety of new topologies to improve the torque characteristics of the MT-FSPM machine. In [8], a simple analysis method

is proposed to determine the optimal combination of the stator pole number and rotor pole number of the machine. The results show that the maximum torque performance can be obtained when the single stator teeth of FSPM motor are divided into four. In [9], a novel hybrid excited multi-tooth FSPM brushless machine is introduced. Although the proposed machine has flux adjustable ability and high torque density, it lacks the analysis of cogging torque and torque ripple performance. In [10], a novel MT-FSPM machine with PMs arrangements is proposed. Although the torque performance is improved, the amount of PM is increased. In addition, HTS materials are widely used in machine due to high conductivity and flux capture capabilities, such as magnets, coils, and bulks, to reduce the leakage flux of the machine [11]. Compared to the HTS machines excited by rotor, the HTS bulk of AC brushless machine excited by stator is located on the stator, and its cooling system is relatively simple, thus improving the reliability of HTS bulks cooling [12].

To attain the optimal design parameter values efficiently and minimize optimization duration, many researchers utilize comprehensive sensitivity analysis. This approach stratifies the sensitivity of design variables, identifying those with higher sensitivity to establish a response surface model for optimization. Conversely, the lower sensitivity parameters are selected as the initial value, or single parameter scanning is performed [13, 14]. In addition, employing a multi-objective genetic algorithm (MOGA) in optimization methods offers high accuracy and optimizes the calculation time. MOGA is used to simulate the natural evolution process, and the optimal solution is obtained by continuous iteration on the basis of finite element method (FEM) [15, 16].

To effectively improve the electromagnetic performance of MT-FSPM machine, a novel MT-FSPM machine with HTS bulks is proposed. In Section 2, the topological structure and

\* Corresponding author: Yunpan Liu (18972039214@163.com).

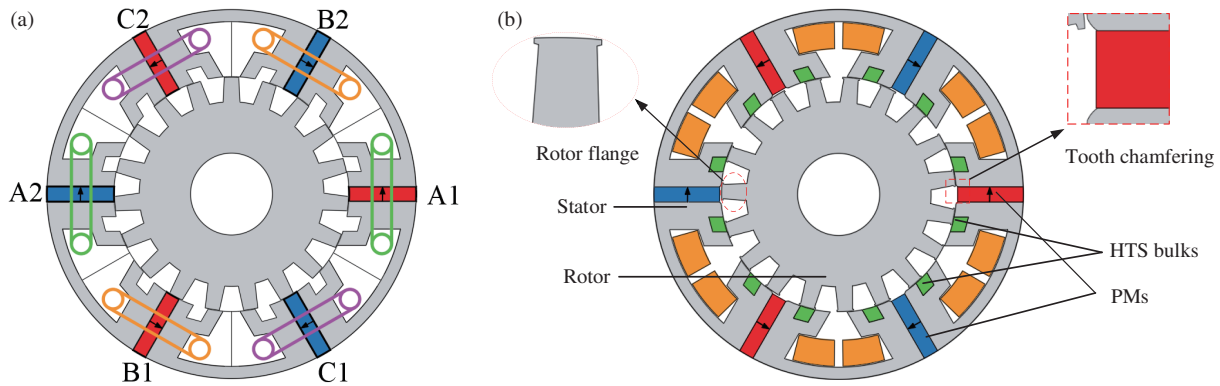


**FIGURE 1.** The topology of MT-FSPM machine. (a) Conventional model. (b) Proposed model.

design parameters of the proposed model are introduced. Section 3 details the acquisition of optimal machine parameters through a combination of response surface method (RSM) and MOGA. Then, two-dimensional finite element models are established, and the electromagnetic performances of conventional model and proposed model are compared in Section 4. Finally, Section 5 presents the conclusions drawn from this paper.

## 2. TOPOLOGY OF MT-FSPM MACHINE

Figure 1(a) depicts the topology of a conventional MT-FSPM machine, whose rotor structure is similar to that of an FSPM machine. Stator core is composed of silicon steel sheets; winding is concentrated winding; and PMs are alternately arranged in the stator teeth. Since the machine requires fewer permanent magnets and produce greater torque than conventional FSPM machine, the number of PMs used in the machine manufacturing process can be reduced, thereby reducing the manufacturing cost of the machine. According to the design principle of FSPM machine, the rotor pole number  $N_r$ , stator pole number  $N_s$ , and phase number  $m$  can be described as:

$$N_s = km \quad (k = 2, 4, 6 \dots) \quad (1)$$

$$N_r = N_s(2n - 1) + 1 \quad (2)$$

where  $k$  denotes a positive even number, and  $n$  represents a positive integer. According to the model shown in Fig. 1(a), the conventional model and proposed model are both three-phase concentrated windings.  $m$  takes 3, and the numbers of stator and rotor teeth are 6 and 19, respectively. Therefore, in this paper,  $n$  is equal to 2.

The proposed topology of MT-FSPM machine with HTS bulks is shown in Fig. 1(b). Specifically, a configuration involving 12 HTS bulks strategically positioned within the stator teeth effectively mitigates flux leakage and enhances the resultant torque output. The methods of stator tooth chamfering and rotor flange structures are adopted to suppress torque ripple, contributing to improved performance. Meanwhile, the remaining structures remain consistent with those in the conventional model.

Table 1 shows the structural parameters of the machine, and the corresponding parameter diagram is shown in Fig. 2(a). The

parameter variable design of rotor pole piece structure and stator tooth chamfering is shown in Fig. 2(b). The extension angle of the rotor teeth is  $\beta_1$ , and the lengths of the pole pieces are  $L_1$  and  $L_2$ , respectively. The radian of the stator tooth chamfering is  $\beta_2$ ; the length is  $L_3$ ; and the length of the extension and contraction of the PM is  $L_4$ . The values of these parameter variables will affect the electromagnetic performance of the machine design. Therefore, this paper selects these six parameters for the subsequent multi-objective optimization aimed at attaining the optimal parameter values.

Due to the Meisner effect, the HTS bulks working below the critical temperature enters the superconducting state, which can effectively suppress the magnetic field penetration. Therefore, the introduction of HTS bulks can reduce the leakage of stator side and enhance the air gap magnetic field density to improve the electromagnetic performance of the machine. Fig. 3 illustrates the composition of the HTS bulk, primarily composed of YBCO HTS material, carbon fiber framework, condensate and vacuum chamber. Notably, the HTS bulks exhibit zero relative permeability. Cooling of the HTS bulk is facilitated via circulating condensate through a liquid tube, with the vacuum chamber serving an insulating function to reduce heat leakage.

## 3. MULTI OBJECTIVE OPTIMIZATION

### 3.1. Comprehensive Sensitivity Analysis

To attain the optimal machine parameters, a multi-objective optimization process was carried out. The schematic of this procedure is depicted in Fig. 4, comprising the subsequent steps.

Step 1: The parametric model is established; the optimal design variables are selected; and the optimization target is determined.

Step 2: The comprehensive sensitivity analysis is carried out to stratify the sensitivity of the design variables. High-sensitivity variables are chosen for multi-objective optimization, and the low sensitivity variable will be selected as the initial value determined when a single parameter scan is performed in Maxwell software.

Step 3: Based on the central composite design, the RSM constructs a fitting model that can reflect the relationship between

Quantity	Value
Number of HTS bulks	12
Number of phase	3
Number of rotor teeth	19
Number of turns/phase	3
Outer radius stator/ $R_1$	144 mm
Inner radius stator/ $R_2$	91.5 mm
Inner radius Rotor/ $R_3$	32 mm
Rotor tooth width/ $w$	7 deg
PM thickness/ $h_1$	11.8 mm
stator yoke thickness/ $h_2$	9.5 mm
Stator tooth height/ $h_3$	7.4 deg
Airgap length/ $g$	0.5 mm
Active axial length	100 mm
Rotation speed/rpm	1500
PM material	NdFeB
HTS material	YBCO

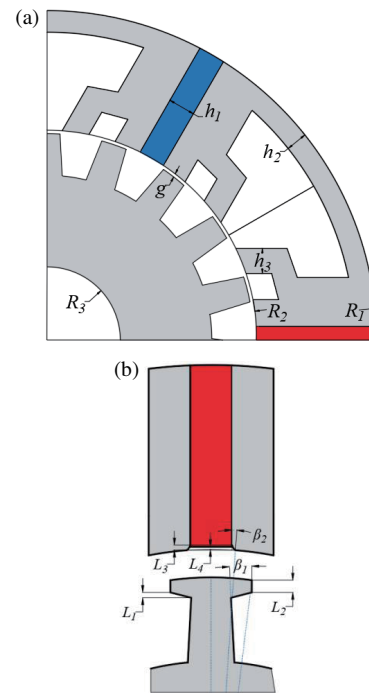


FIGURE 2. Parameters design. (a) Conventional model. (b) Dimensional parameters for a stator and rotor pole.

TABLE 1. Structural parameters of MT-FSPM machine with HTS bulks.

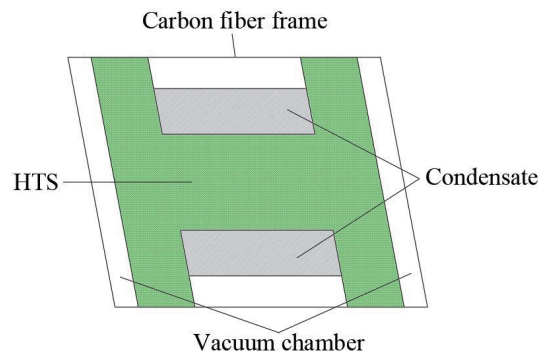


FIGURE 3. HTS bulk.

the experimental variables and the response variables [17, 18]. The MOGA forms the Pareto front and provides the choice of multiple trade-off solutions in the design space. By combining MOGA and RSM, their respective advantages can be fully utilized to achieve global search and local optimization of machine design parameters, reduce computational costs, and effectively deal with multi-objective problems to achieve the desired design goals.

Step 4: The conventional and proposed two-dimensional finite element models are constructed to compare the critical electromagnetic properties.

This paper aims to optimize the average output torque and minimize torque ripple of the machine. To achieve this target, six key variables outlined in Fig. 2(b) are identified as the design variables for optimization. Before the response surface analysis of the two-dimensional finite element model, it is necessary to evaluate the sensitivity of the designed vari-

ables to obtain the sensitivity factor  $S(n_i)$  of variable  $n_i$  to a certain optimization objective. Considering the two optimization objectives, a comprehensive evaluation of each optimization variable is carried out using the weight coefficient method. Therefore, this paper introduces a comprehensive sensitivity  $S_{com}(n_i)$ , which can be described as:

$$S_{com}(n_i) = w_1 |S_{avg}(n_i)| + w_2 |S_{rip}(n_i)| \quad (3)$$

$$w_1 + w_2 = 1 \quad (4)$$

where  $S_{avg}$  and  $S_{rip}$  are respectively the sensitive factors of optimization variable  $n_i$  for the two optimization objectives,  $w_1 = 0.5$  and  $w_2 = 0.5$ . The sensitivity stratification results are shown in Table 2. According to the calculation of the comprehensive sensitivity coefficient, variables  $\beta_1$  and  $L_4$  have the sensitivity coefficients of 0.615 and 0.361, respectively, and are divided into high-level sensitivity variables, which have a great influence on the optimization goal. Therefore, further op-

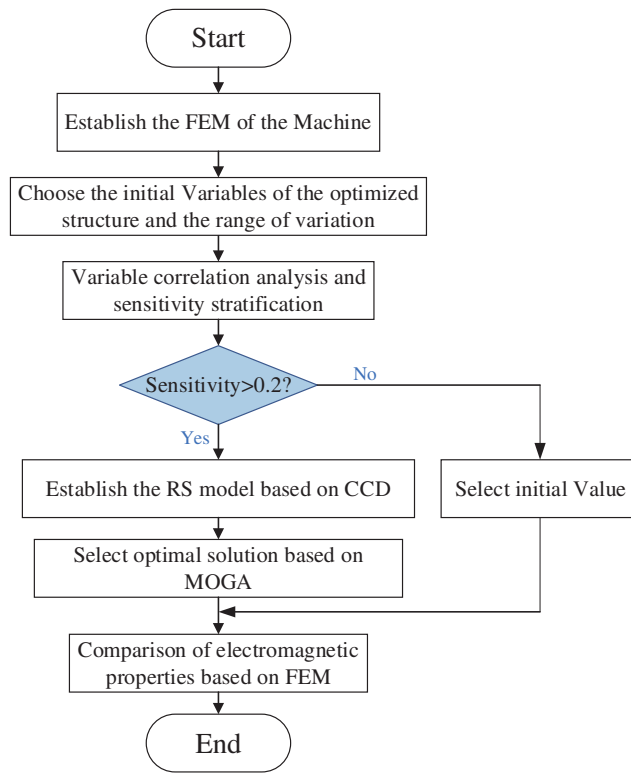


FIGURE 4. Flow chart of optimization design.

TABLE 2. Comprehensive sensitivity indexes.

Design variables	Design objectives		Sensitivity $S_{com}(n_i)$	
	$ S_{avg}(n_i) $ $w_1 = 0.5$	$ S_{rip}(n_i) $ $w_2 = 0.5$		
High	$n_1/\beta_1$	0.883	0.347	0.615
Level	$n_2/L_4$	0.351	0.371	0.361
	$n_3/L_1$	0.025	0.228	0.127
Low	$n_4/L_2$	0.237	0.047	0.142
Level	$n_5/L_3$	0.048	0.104	0.076
	$n_6/\beta_2$	0.001	0.068	0.035

timization will be carried out to determine the optimal value, and low level sensitivity variables are selected as initial values.

### 3.2. RSM

RSM is a statistical modeling technique that aims to study and optimize multiple factors that affect the results (responses). By designing experiments to observe the influence of different input variable levels on the output variables, the advantage is that it can comprehensively consider the influence of multiple factors on the results, and establish mathematical models to describe these relationships and provide reliable predictions. This method helps to understand and optimize complex systems and provides effective support for machine design, process improvement or system performance optimization. The experimental sample dataset in this paper is formulated utilizing the principles of the central composite design (CCD), which can be

expressed as:

$$y = a_0 + \sum_{i=1}^3 a_i n_i + \sum_{i=1}^3 a_{ii} n_i^2 + \sum_{i=1}^2 \sum_{j>i}^3 a_{ij} n_j + e_r \quad (5)$$

where  $y$  is the optimization objective,  $a$  the undetermined coefficient,  $n$  is the optimization variables, and  $e_r$  the fitting error.

The response surface models for torque average ( $T_{avg}$ ) and torque ripple ( $T_{rip}$ ) were developed utilizing Kriging-SMA, focusing on two variables:  $\beta_1$  and  $L_4$ , which possess notably high sensitivity coefficients. As shown in Fig. 5(a),  $T_{avg}$  will gradually decrease with the increase of  $\beta_1$  and  $L_4$ . Conversely, Fig. 5(b) demonstrates that  $T_{rip}$ 's trend initially rises and subsequently declines with the increase in  $\beta_1$ , indicating a preference for smaller values of  $\beta_1$ . Notably, with smaller values of  $\beta_1$ ,  $T_{rip}$  generally shows a progressive decrease with the rise of  $L_4$ ,

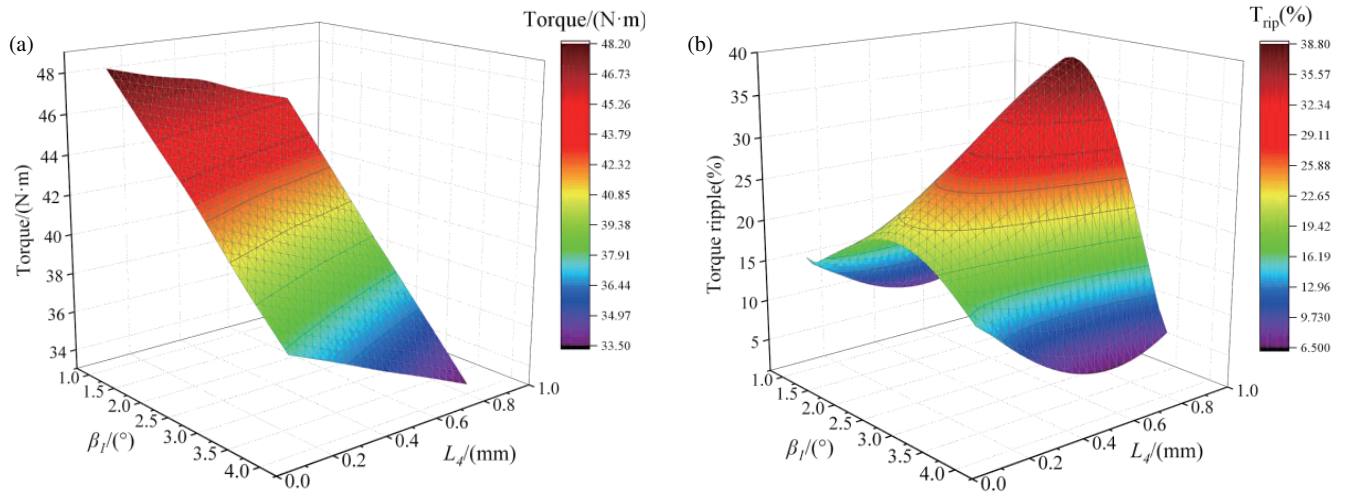


FIGURE 5. Effect of  $\beta_1$  and  $L_4$  optimization on torque profile. (a)  $T_{avg}$ . (b)  $T_{rip}$ .

TABLE 3. Optimal parameters of MTFSPM machine.

Parameter	Variation range	Value	
		Initial	Optimal
$L_1$	[0 mm, 4 mm]	0.8 mm	
$L_2$	[0 mm, 4 mm]	2.2 mm	
$L_3$	[0 mm, 3 mm]	1.4 mm	
$L_4$	[0 mm, 1 mm]	1.4 mm	0.9 mm
$\beta_1$	[1 deg, 5 deg]	1.8 deg	1.2 deg
$\beta_2$	[0 deg, 3 deg]	0.8 deg	

but a larger  $L_4$  diminishes the  $T_{avg}$ . Therefore, the value of  $L_4$  needs to be further optimized to obtain better electromagnetic performance.

### 3.3. MOGA Optimization

To attain the global optimum for the dual objectives, the application of MOGA in the multi-objective optimization design of the MT-FSPM machine is pivotal. MOGA stands out due to its exceptional accuracy, rapid convergence, and minimal need for parameter fine-tuning, effectively addressing multi-objective optimization challenges. This study leverages the genetic algorithm to derive optimized variables, aiming to maximize the average output torque while minimizing torque ripple. The objective functions can be written as follows [19]:

$$\begin{cases} \text{Obj} : \begin{cases} \text{Max}(T_{avg}(n)) \\ \text{Min}(T_{rip}(n)) \end{cases} \\ \text{s.t.} : n_{\min} < n_i < n_{\max} \quad (i = 1, 2, 3) \end{cases} \quad (6)$$

where the maximum  $T_{avg}(n)$  and minimum  $T_{rip}(n)$  are the optimization objectives, respectively.

Figure 6(a) depicts the convergence of the average output torque to 478 N·m within 11 iterations. In the range of 0 to 5500 points, the average torque shows a wide and erratic oscillation, which is due to the existence of multiple local optimal

solutions in the search space, resulting in the optimization algorithm hovering between these points. This indicates that a small change in the design parameters may cause a large change in the average torque. In addition, the interaction between different design parameters may also lead to complex behaviors of the system, which may lead to erratic oscillation of the average torque. Fig. 6(b) illustrates the convergence of torque ripple to 0.038. According to the results after MOGA optimization, the optimized variable values are shown in Table 3.

## 4. SIMULATION ANALYSIS

A two-dimensional finite element model has been created in Maxwell software based on the outcomes of multi-objective optimization [20]. This model is utilized for comparative analysis between the optimized conventional and proposed models. The comparison and analysis encompass the magnetic field distribution, back electromotive force (EMF) waveform, and torque performance.

### 4.1. Magnetic Field Analysis

MT-FSPM machine adopts tangential alternating magnetization. The flux generated by two adjacent permanent magnets will pass through the air gap together, resulting in the saturation of air gap flux density. Excessive saturation can increase the

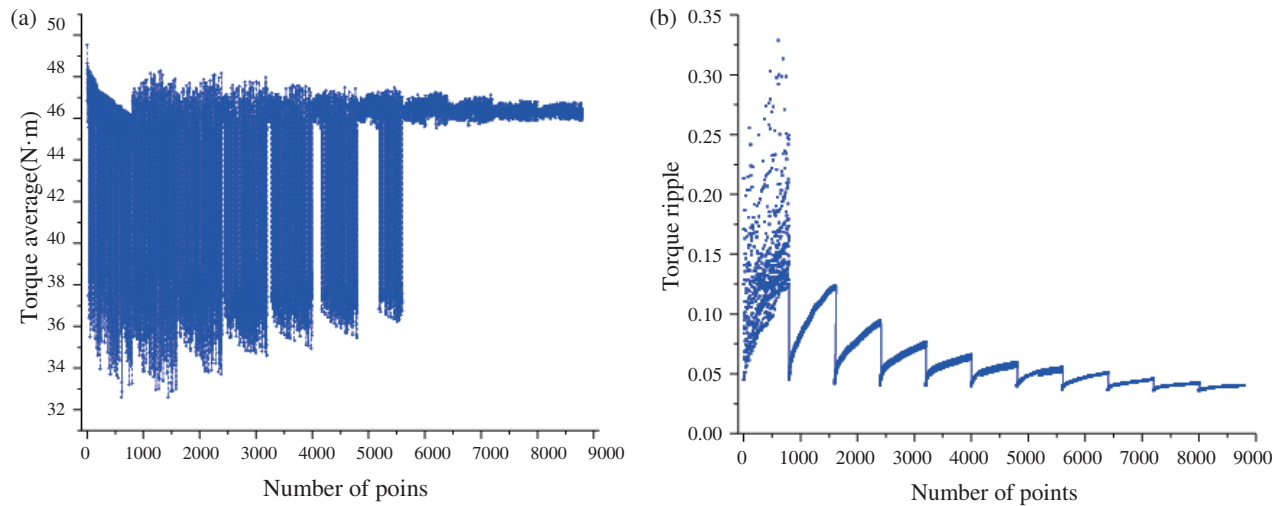


**FIGURE 6.** Convergence of the objective function. (a) Convergence of torque average. (b) Convergence of torque ripple.

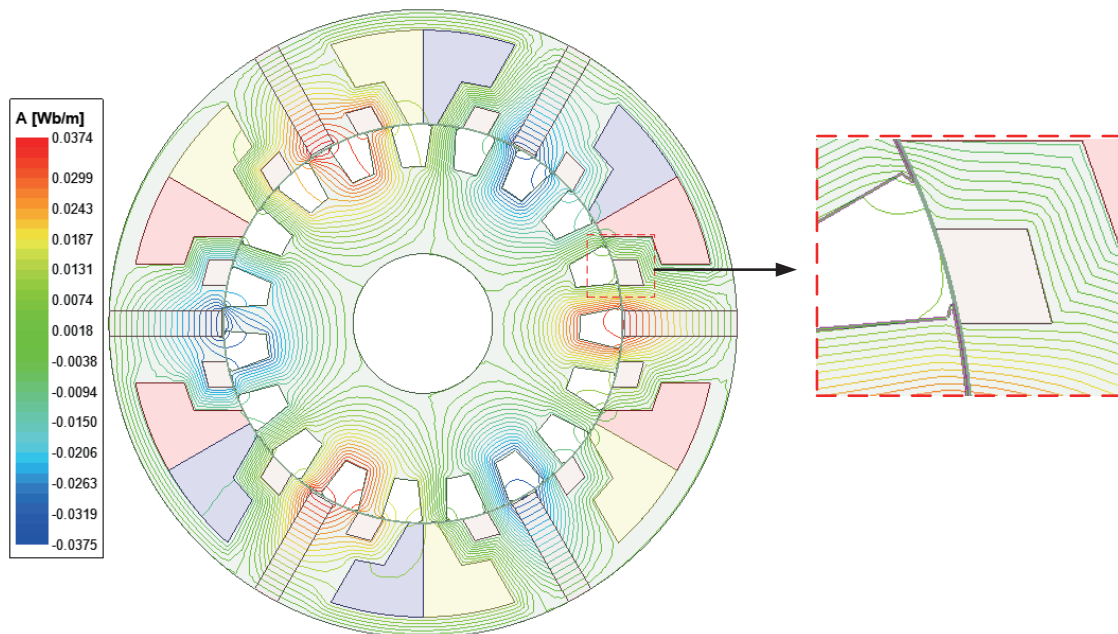


**FIGURE 7.** Flux distributions under no-load condition.

output torque of the machine, but it will inevitably lead to serious leakage of the machine. Therefore, to address this problem, as depicted in Fig. 7, a solution has been implemented wherein the air gap of the stator teeth is arranged with 12 HTS bulks. It optimizes the machine's  $T_{avg}$  by minimizing the undesired magnetic leakage while ensuring that the magnetic lines bypass the HTS region which effectively mitigates the leakage magnetic phenomenon in this area.

The magnetic flux density cloud map of the conventional machine is illustrated in Fig. 8(a). Due to the salient pole structure of the stator and rotor teeth of the MT-FSPM machine, a magnetic flux concentration effect occurs in the tooth region. This situation leads to a local saturation phenomenon in the tooth area of conventional machines. In contrast, as depicted in Fig. 8(b), the proposed machine employs stator tooth chamfer-

ing and rotor flange structures, resulting in a slightly increased local saturation phenomenon but with minimal overall impact. Nevertheless, in practical design, it should be noted that this local saturation effect may adversely affect the loss, temperature rise, and efficiency of the machine.

#### 4.2. No-Load Back EMF

The no-load back-EMF plays a crucial role in assessing machine performance. FSPM machines, with winding consistency and complementarity, exhibit significantly lower total harmonic distortion (THD) than traditional PM synchronous machines [21]. This attribute results in a high degree of sinusoidal purity. As illustrated in Fig. 9(a), the proposed model showcases an 18.9% increase in back-EMF amplitude, rising

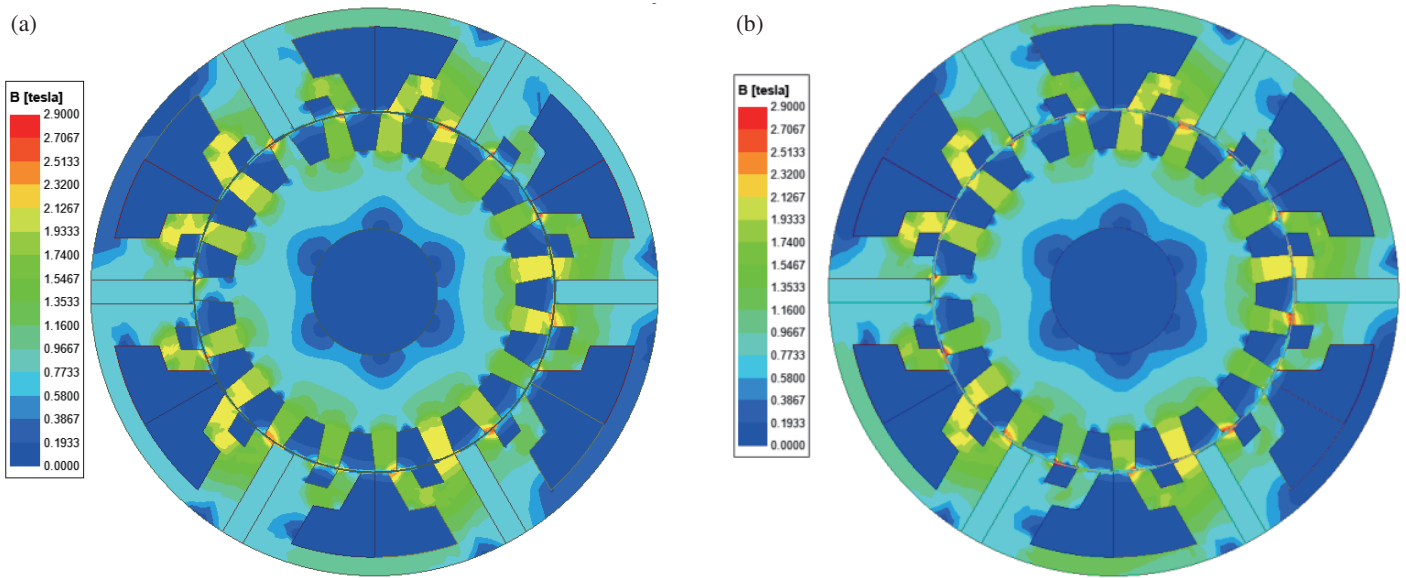


FIGURE 8. Magnetic flux density cloud map. (a) Conventional. (b) Proposed.

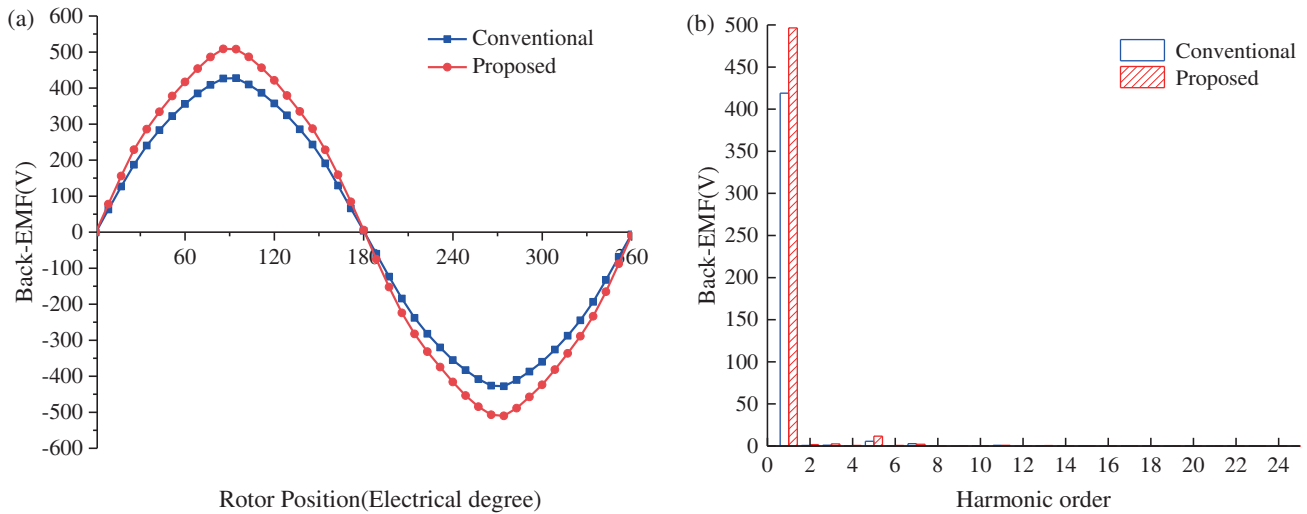


FIGURE 9. BackEMF of MT-FSPM machine (a) Waveform. (b) Harmonic spectra.

from 427.5 V to 508.1 V, outperforming the conventional MT-FSPM machine.

THD is a metric that assesses the quality of a signal or waveform. It signifies the ratio between the total sum of harmonic components within the waveform and the fundamental frequency. It is typically expressed as:

$$THD = \frac{\sqrt{\sum_{m=2}^{\infty} B_m^2}}{B_1} \times 100\% \quad (7)$$

where  $B_m$  is the  $k$ th harmonic amplitude, and  $B_1$  is the amplitude of fundamental wave.

The distribution of individual harmonic orders following the Fourier decomposition of the no-load back EMF is depicted in Fig. 9(b). It is suggested that the fundamental amplitude of the

back EMF of the model increases from 418.9 V to 496.4 V, an increase of 18.5%. Although the 5th harmonic component has increased, the THD has increased from 1.5% to 2.5%, but it still maintains a high sinusoidal degree, ensuring the machine's reliability and stability during operation.

### 4.3. Torque Performance

The primary drawback of a double salient pole structure in a permanent magnet machine is larger cogging torque. The cogging torque cycle ( $N_p$ ) for a machine with a pole-pair number ( $P$ ) can be defined as follows [22]:

$$N_p = \frac{360P}{LCM(N_s, N_r)} \quad (8)$$

where  $LCM(N_s, N_r)$  is the least common multiple between  $N_s$  and  $N_r$ , and  $N_p$  equals  $60^\circ$ .

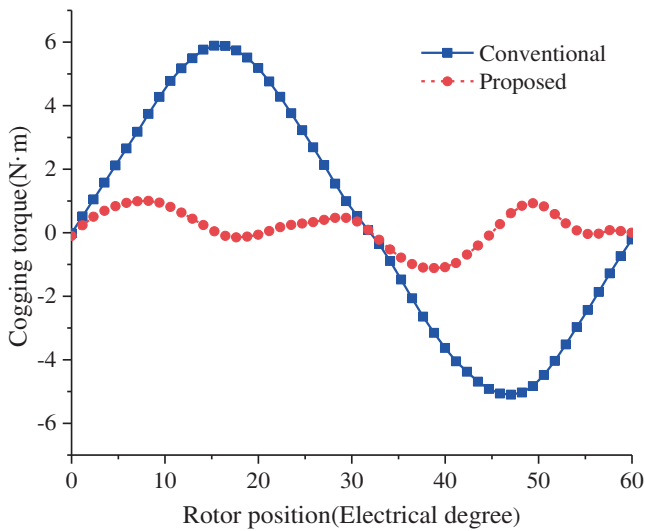


FIGURE 10. Cogging torque.

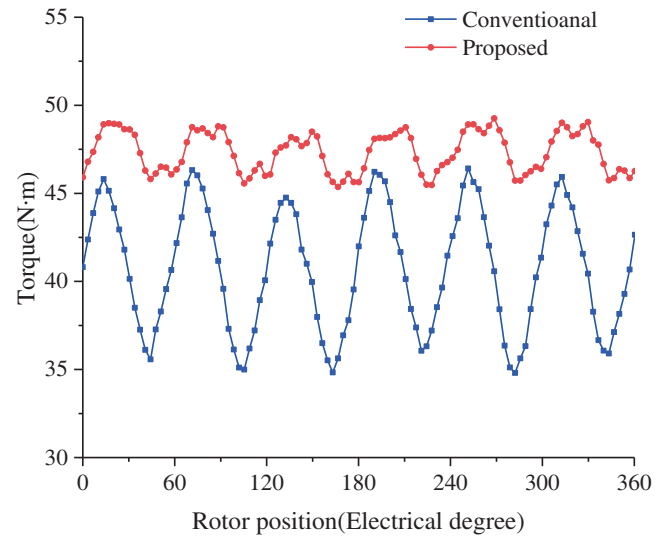


FIGURE 11. Output torque.

Parameter	Conventional	Proposed
Copper loss (W)	427.93	456.51
Core loss (W)	332.07	393.97
Eddy current loss (W)	116.16	199.60
Total loss (W)	876.16	1050.08
Output power (W)	6391.72	7438.74
Efficiency	87.94%	87.62%

TABLE 4. Various losses, output power and efficiency.

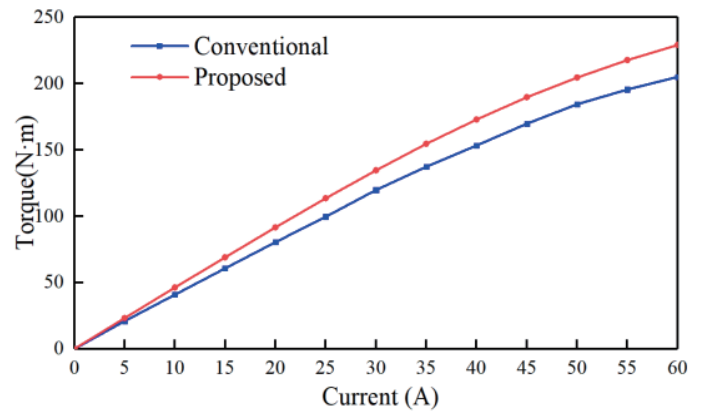


FIGURE 12. Output torque versus current in two machines.

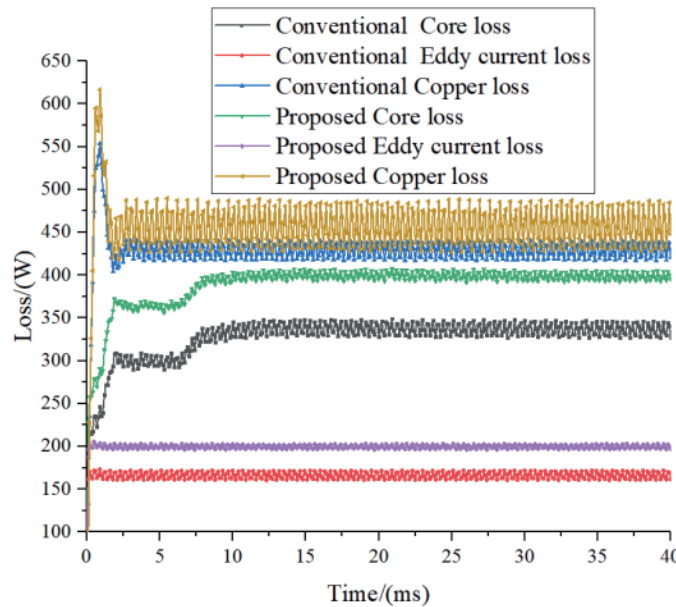


FIGURE 13. Loss comparison.

In Fig. 10, employing the stator and rotor tooth structure has significantly mitigated the cogging torque amplitude in the proposed machine. The proposed model has effectively minimized the machine's vibration and noise.

In Fig. 11, a comparison of the output torque characteristics of the MT-FSPM machine is depicted. The conventional machine exhibits an output torque of 40.69 N·m, whereas the proposed MT-FSPM machine incorporating HTS bulks shows an average output torque of 47.36 N·m, marking a notable 16.4% increase. Moreover, the output torque ripple has been reduced from 26.5% to 5.4%, indicating a 79.6% decrease. The results show that the optimized MT-FSPM machine has more stable torque transmission capacity than the conventional machine.

#### 4.4. Overload Performance

To compare the disparity in overload capacity between the two models, Fig. 12 illustrates the curves of electromagnetic torque and current. Because the proposed model is almost consistent with the conventional model in terms of saturation phenomenon, the overload capacity of the proposed model is similar to that of the conventional model. In a wide load current range, the proposed model can still produce high output torque and meet the demand for high output torque application.

#### 4.5. Loss and Efficiency

In Fig. 13, the losses of the two models are compared and analyzed. Compared with the conventional model, the proposed model shows a larger loss, increasing from 876.16 W to 1050.08 W, and the specific parameter values are shown in Table 4. However, the model has a higher output torque capability to achieve higher output power. The efficiency of proposed model is 87.62%, which is almost consistent with the 87.94% of the conventional model. Therefore, although the loss of the proposed model increases, it can still meet the operating requirements of the MT-FSPM machine.

## 5. CONCLUSION

This paper introduces a novel MT-FSPM machine with HTS bulks. The torque ripple is effectively reduced by the rotor pole shoe and stator tooth chamfering, and the magnetic flux leakage is obviously restricted by arranging HTS bulks in stator teeth. Employing multi-objective optimization leads to the determination of optimized machine variables. Utilizing FEM analysis, the electromagnetic performance of the optimized machine exhibits significant enhancement in contrast to the conventional model. The no-load back-EMF amplitude is increased by 18.9%, the average output torque increased by 16.4%, the torque ripple reduced by 79.6%, and the efficiency is almost consistent.

## REFERENCES

- [1] Lee, C. H. T., K. T. Chau, C. Liu, T. W. Ching, and M. Chen, "A new magnetless flux-reversal HTS machine for direct-drive application," *IEEE Transactions on Applied Superconductivity*, Vol. 25, No. 3, 1–5, Jun. 2015.
- [2] Balachandran, T., D. Lee, N. Salk, J. Xiao, and K. S. Haran, "Evaluation and mitigation of AC losses in a fully superconducting machine for wind turbine applications," *IEEE Transactions on Applied Superconductivity*, Vol. 30, No. 4, 1–5, Jun. 2020.
- [3] Jing, L., Z. Min, Z. Kui, K. Yang, and R. Qu, "A flux-switching permanent magnet machine with HTS bulks and radially magnetized PMs arranged," *IEEE Transactions on Applied Superconductivity*, Vol. 33, No. 5, 1–5, Aug. 2023.
- [4] Dong, Y., X. Li, and X. Feng, "Investigation of a novel radial partitioned stator HTS-excitation flux-switching machine," *IEEE Transactions on Applied Superconductivity*, Vol. 31, No. 5, 1–5, Aug. 2021.
- [5] Chen, J. T., Z. Q. Zhu, S. Iwasaki, and R. P. Deodhar, "A novel E-core switched-flux PM brushless AC machine," *IEEE Transactions on Industry Applications*, Vol. 47, No. 3, 1273–1282, May-Jun. 2011.
- [6] Li, Y. and W. Xu, "Optimization and performance analysis of E-core and C-core flux-switching permanent-magnet machines for electric vehicle applications," in *2014 17th International Conference on Electrical Machines and Systems (ICEMS)*, 53–59, Hangzhou, China, 2014.
- [7] Zhu, Z. Q., J. T. Chen, Y. Pang, D. Howe, S. Iwasaki, and R. Deodhar, "Analysis of a novel multi-tooth flux-switching PM brushless AC machine for high torque direct-drive applications," *IEEE Transactions on Magnetics*, Vol. 44, No. 11, 4313–4316, Nov. 2008.
- [8] Chen, J. T., Z. Q. Zhu, and D. Howe, "Stator and rotor pole combinations for multi-tooth flux-switching permanent-magnet brushless AC machines," *IEEE Transactions on Magnetics*, Vol. 44, No. 12, 4659–4667, Dec. 2008.
- [9] Zhang, Z., J. Chen, and X. Liu, "Hybrid-excited multi-tooth flux switching brushless machines for EV propulsion," in *2019 IEEE Transportation Electrification Conference and Expo (ITEC)*, 1–5, 2019.
- [10] Wang, Y. and Z. Deng, "A multi-tooth fault-tolerant flux-switching permanent-magnet machine with twisted-rotor," *IEEE Transactions on Magnetics*, Vol. 48, No. 10, 2674–2684, Oct. 2012.
- [11] Messina, G., M. Yazdani-Asrami, F. Marignetti, and A. D. Corte, "Characterization of HTS coils for superconducting rotating electric machine applications: Challenges, material selection, winding process, and testing," *IEEE Transactions on Applied Superconductivity*, Vol. 31, No. 2, 1–10, Mar. 2021.
- [12] Lu, M. and R. Cao, "Comparative investigation of high temperature superconducting linear flux-switching motor and high temperature superconducting linear switched reluctance motor for urban railway transit," *IEEE Transactions on Applied Superconductivity*, Vol. 31, No. 5, 1–5, Aug. 2021.
- [13] Xiang, Z., X. Zhu, L. Quan, Y. Du, C. Zhang, and D. Fan, "Multilevel design optimization and operation of a brushless double mechanical port flux-switching permanent-magnet motor," *IEEE Transactions on Industrial Electronics*, Vol. 63, No. 10, 6042–6054, Oct. 2016.
- [14] Li, X., Z. Xue, X. Yan, L. Zhang, W. Ma, and W. Hua, "Low-complexity multivector-based model predictive torque control for PMSM with voltage preselection," *IEEE Transactions on Power Electronics*, Vol. 36, No. 10, 11 726–11 738, Oct. 2021.
- [15] Guazzelli, P. R. U., W. C. de Andrade Pereira, C. M. R. de Oliveira, and A. G. de Castro, "Weighting factors optimization of predictive torque control of induction motor by multiobjective genetic algorithm," *IEEE Transactions on Power Electronics*, Vol. 34, No. 7, 6628–6638, Jul. 2019.

- [16] Hasanien, H. M., A. S. Abd-Rabou, and S. M. Sakr, "Design optimization of transverse flux linear motor for weight reduction and performance improvement using response surface methodology and genetic algorithms," *IEEE Transactions on Energy Conversion*, Vol. 25, No. 3, 598–605, Sep. 2010.
- [17] Islam, S., B. Halder, and A. R. Ali, "Optical and rogue type soliton solutions of the  $(2 + 1)$  dimensional nonlinear heisenberg ferromagnetic spin chains equation," *Scientific Reports*, Vol. 13, No. 1, 9906, 2023.
- [18] Abo-Seida, O. M., N. T. M. El-dabe, A. R. Ali, and G. A. Shalaby, "Cherenkov FEL reaction with plasma-filled cylindrical waveguide in fractional D-dimensional space," *IEEE Transactions on Plasma Science*, Vol. 49, No. 7, 2070–2079, Jul. 2021.
- [19] Zhao, W., A. Ma, J. Ji, X. Chen, and T. Yao, "Multiobjective optimization of a double-side linear Vernier PM motor using response surface method and differential evolution," *IEEE Transactions on Industrial Electronics*, Vol. 67, No. 1, 80–90, Jan. 2020.
- [20] Mahmuda Maya, M. U., M. N. Alam, and A. R. Ali, "Influence of magnetic field on MHD mixed convection in lid-driven cavity with heated wavy bottom surface," *Scientific Reports*, Vol. 13, No. 1, 18959, 2023.
- [21] Liu, Y., H. Yu, and Y. Wang, "Establishment of a new dual rotor flux switching motor magnetic circuit model and optimization of no-load back EMF," *IEEE Transactions on Magnetics*, Vol. 55, No. 12, 1–5, Dec. 2019.
- [22] Jing, L. and Z. Min, "A novel flux-switching permanent magnet machine with dual sets of magnet arrangements," *Journal of Electrical Engineering & Technology*, Vol. 18, No. 1, 299–306, Jan. 2023.